



**HAL**  
open science

## **Fine-regolith production on asteroids controlled by rock porosity**

S Cambioni, M Delbo, G Poggiali, C Avdellidou, A J Ryan, J D P Deshapriya, E Asphaug, R.-L Ballouz, M A Barucci, C A Bennett, et al.

► **To cite this version:**

S Cambioni, M Delbo, G Poggiali, C Avdellidou, A J Ryan, et al.. Fine-regolith production on asteroids controlled by rock porosity. *Nature*, 2021, 10.1038/s41586-021-03816-5 . hal-03450468

**HAL Id: hal-03450468**

**<https://hal.science/hal-03450468v1>**

Submitted on 18 Nov 2022

**HAL** is a multi-disciplinary open access archive for the deposit and dissemination of scientific research documents, whether they are published or not. The documents may come from teaching and research institutions in France or abroad, or from public or private research centers.

L'archive ouverte pluridisciplinaire **HAL**, est destinée au dépôt et à la diffusion de documents scientifiques de niveau recherche, publiés ou non, émanant des établissements d'enseignement et de recherche français ou étrangers, des laboratoires publics ou privés.

1 **Fine-regolith production on asteroids controlled by rock porosity**

2

3 S. Cambioni<sup>1,2</sup>, M. Delbo<sup>3</sup>, G. Poggiali<sup>4</sup>, C. Avdellidou<sup>3</sup>, A.J. Ryan<sup>1</sup>, J.D.P. Deshapriya<sup>5</sup>, E.  
4 Asphaug<sup>1</sup>, R.-L. Ballouz<sup>1</sup>, M.A. Barucci<sup>5</sup>, C.A. Bennett<sup>1</sup>, W.F. Bottke<sup>6</sup>, J.R. Brucato<sup>4</sup>, K.N.  
5 Burke<sup>1</sup>, E. Cloutis<sup>7</sup>, D.N. DellaGiustina<sup>1</sup>, J.P. Emery<sup>8</sup>, B. Rozitis<sup>9</sup>, K.J. Walsh<sup>6</sup>, and D.S.  
6 Lauretta<sup>1</sup>

7

8 (1) Lunar and Planetary Laboratory, University of Arizona, Tucson, AZ, USA; (2) Division of  
9 Geological and Planetary Sciences, California Institute of Technology, Pasadena, CA, USA; (3)  
10 Université Côte d'Azur, Observatoire de la Côte d'Azur, CNRS, Laboratoire Lagrange, Nice,  
11 France; (4) INAF – Osservatorio Astrofisico di Arcetri, Florence, Italy; (5) LESIA, Observatoire  
12 de Paris, Université PSL, CNRS, Sorbonne Université, Univ. Paris Diderot, Sorbonne Paris Cité,  
13 Meudon, France; (6) Southwest Research Institute, Boulder, CO, USA; (7) Department of  
14 Geography, University of Winnipeg, Winnipeg, MB, R3B 2E9, Manitoba, Canada; (8)  
15 Department of Astronomy and Planetary Science, Northern Arizona University, Flagstaff, AZ,  
16 USA; (9) School of Physical Sciences, The Open University, Milton Keynes, UK.

17

18 **Spacecraft missions observed regolith blankets consisting of unconsolidated sub-centimetre**  
19 **particles on stony asteroids<sup>1-3</sup>. Telescopic data suggested regolith blankets to be present**  
20 **also on carbonaceous asteroids, including (101955) Bennu<sup>4</sup> and (162173) Ryugu<sup>5</sup>. However,**  
21 **despite observations of processes capable of comminuting boulders into unconsolidated**  
22 **materials, such as meteoroid bombardment<sup>6,7</sup> and thermal cracking<sup>8</sup>, Bennu and Ryugu**  
23 **lack extensive areas covered in sub-centimetre particles<sup>9,7</sup>. Here we report an inverse**

24 **correlation between the local abundance of sub-centimetre particles and the porosity of**  
25 **rocks on Bennu. We interpret this finding to mean that accumulation of unconsolidated**  
26 **sub-centimetre particles is frustrated where the rocks are highly porous, which appears to**  
27 **be most of the surface<sup>10</sup>: these rocks are compressed rather than fragmented by meteoroid**  
28 **impacts, consistent with laboratory experiments<sup>11,12</sup>, and thermal cracking proceeds more**  
29 **slowly than in denser rocks. We infer that regolith blankets are uncommon on**  
30 **carbonaceous asteroids, which are the most numerous of all asteroid types<sup>13</sup>. By contrast,**  
31 **these terrains should be common on stony asteroids, which have less porous rocks and are**  
32 **the second-most populous group by composition<sup>13</sup>. The higher porosity of carbonaceous**  
33 **asteroid materials may have aided in their compaction and cementation to form breccias,**  
34 **which dominate the carbonaceous chondrite meteorites<sup>14</sup>.**

35  
36 Between April and June 2019, the Origins, Spectral Interpretation, Resource Identification, and  
37 Security-Regolith Explorer (OSIRIS-REx) Thermal Emission Spectrometer<sup>15</sup> (OTES) measured  
38 thermal infrared emission spectra from Bennu's surface at different local times of day. These  
39 spectra are a function of surface temperatures, which vary throughout the day and night  
40 differently depending on surface roughness and thermal inertia. Roughness ( $\theta$ ) is due to surface  
41 irregularities that are not resolved in global topography but still affect temperatures due to  
42 shadows and self-heating<sup>16</sup>. Thermal inertia ( $\Gamma$ ) measures materials' resistance to temperature  
43 change; it is determined by thermal conductivity  $\kappa$ , heat capacity  $c_p$ , and bulk density  $\rho$   
44 ( $\Gamma=[\kappa c_p \rho]^{1/2}$ ), and allows distinguishing different geological units, such as fine regolith from  
45 rocks.

46

47 Here fine regolith means unconsolidated particles of size smaller than the e-folding depth of the  
48 diurnal thermal wave ( $l_s$ , a few centimetres on Bennu<sup>10</sup>), while rocks are defined as every  
49 competent surface material of size  $D_R > l_s$ . The thermal inertia of fine regolith ( $\Gamma_P$ ) is lower than  
50 that of rocks of same composition ( $\Gamma_R$ ) because radiative thermal conduction between particles is  
51 less efficient than phononic heat transfer within an individual particle or rock<sup>16</sup>. Thus, fine  
52 regolith is hotter than rocks during the day, and vice versa during the night. Both fine regolith  
53 and rocks contribute to the infrared emission proportionally to their surface abundances  $\alpha$  and  
54  $(1-\alpha)$ , respectively<sup>17</sup>.

55  
56 To distinguish fine regolith from rocks on Bennu, we use a machine learning method<sup>17</sup> that  
57 explores all possible combinations of the spectral signals of fine regolith and rocks as a function  
58 of their surface abundance, roughness and respective thermal inertia until the OTEs daytime and  
59 night-time observations are simultaneously fitted (Methods). We use our method to derive  $\Gamma_P$ ,  
60  $\Gamma_R$ , and  $\alpha$  in 122 quasi-randomly-distributed OTEs footprints (spots) of  $\sim 40$  m in diameter  
61 (Supplementary Table 1; Extended Data Figure 1). These spots include the two best-observed  
62 areas on Bennu: the designated backup and primary sampling sites of OSIRIS-REx, respectively  
63 called Osprey and Nightingale.

64  
65 We find that  $\alpha$  varies between a few and several tens of percent (Figure 1) and there is less fine  
66 regolith at Osprey than at Nightingale, consistent with the surface abundance of unresolved  
67 materials seen in PolyCam images (Extended Data Figure 2). The values of  $\alpha$  are also consistent  
68 with the surface abundance of unresolved materials in PolyCam images at coarser spatial  
69 resolution (Methods; Extended Data Figure 3). The measured  $\Gamma_R$  encompasses a continuum of

70 values between  $\sim 250 \text{ Jm}^{-2}\text{K}^{-1}\text{s}^{-0.5}$ , close to that derived<sup>18,19</sup> for Ryugu's boulders, and  $>1,000$   
71  $\text{Jm}^{-2}\text{K}^{-1}\text{s}^{-0.5}$ , close to that of CM2 carbonaceous chondrites<sup>20</sup> of composition analogous to the  
72 one spectroscopically inferred for Bennu<sup>21</sup>. For  $\alpha \approx 0$ ,  $\Gamma_R$  is within the range of thermal inertia  
73 values derived by a previous study<sup>10</sup>, which assumed that the surface in the OTES spot is  
74 composed of a single geological unit.

75

76 We observe a direct correlation between  $\Gamma_R$  and  $\alpha$  (Figure 1), with Spearman correlation  
77 coefficient  $R=0.56 \pm 0.06$  and a probability of non-correlation  $p < 4 \times 10^{-3}$  (Methods; Extended Data  
78 Figure 4). The correlation is robust ( $R=0.54 \pm 0.07$ ;  $p < 0.05$ ) when we reject spots where the  
79 thermophysical model may confuse very low- $\Gamma_R$  boulders as fine-regolith-covered areas  
80 (Methods; Figure 1). The correlation is also robust against the choice of a model parameter that  
81 represents the fine-regolith macroporosity (Methods; Extended Data Figure 5). Additionally, we  
82 demonstrate that the correlation is not an artefact of thermophysical modelling (Methods;  
83 Extended Data Figure 6). Finally, we do not see an inverse correlation between  $\alpha$  and the size of  
84 the largest boulders in the OTES spots (Methods; Extended Data Figure 7), thus ruling out that  
85 the  $\Gamma_R$ - $\alpha$  correlation is due to boulders' sizes (large boulders may have lower  $\Gamma_R$  than smaller  
86 ones<sup>10</sup>).

87

88 Because fine regolith is more abundant where rocks have higher  $\Gamma_R$  (Figure 1), and  $\Gamma_R$  is a  
89 monotonically decreasing<sup>19</sup> function of rock porosity (Methods), we deduce that the surface  
90 abundance of fine regolith is lower where the nearby rocks are more porous (Figure 1).

91

92 We argue that the correlation of Figure 1 can be explained by the dependence of regolith-  
93 forming processes, i.e., collisional and thermal fragmentation of rocks, on rock porosity.

94

95 Collisional fragmentation is driven by meteoroid impacts, craters from which were observed<sup>6</sup> on  
96  $D_R \gg 1_s$  rocks. Craters on rough-textured rocks were measured, by means of the OSIRIS-REx  
97 Laser Altimeter, to have a higher depth-to-diameter ratio than those on smoother rocks<sup>6</sup>. Because  
98 crater depth-to-diameter ratio typically increases with increasing target porosity<sup>11,22</sup>, we deduce  
99 that Bennu hosts rocks of different porosities, consistent with Figure 1 and ref. 10, but  
100 independently of OTEs data. Impact experiments show that: (i) a lower-porosity rock requires a  
101 lower energy per unit mass to be broken than a higher-porosity rock, because in the latter impact  
102 energy is spent on pore-space collapse<sup>11</sup> and compaction<sup>12</sup> during initial crater formation; (ii)  
103 crater ejecta's mass, which could partially contribute to fine regolith, decreases with increasing  
104 target porosity<sup>11</sup>; and (iii) craters formed on low-porosity ( $\Phi \approx 25\%$ ) rock simulants of Bennu's  
105 composition have spalls<sup>23</sup>, which increase fragment production. Conversely, spalling was rarely  
106 observed around craters on Bennu's rocks<sup>6</sup>. We deduce that collisional fragmentation increases  
107 with decreasing rock porosity and is frustrated on Bennu's rocks, which typically have  $\Phi > 25\%$   
108 (Figure 2).

109

110 Asteroids' rocks can develop fatigue fractures to release mechanical stresses generated by diurnal  
111 temperature cycling<sup>24</sup>. It is postulated that these fractures grow until breaking the host rocks,  
112 thereby producing regolith<sup>24</sup>. Exfoliation fractures with sizes between a few centimetres and few  
113 metres were observed<sup>8</sup> on Bennu, consistent with the aforementioned process. To investigate  
114 regolith formation by thermal fatigue, we model (Methods) the time to break two rocks on Bennu

115 that have porosity  $\Phi=20\%$  and  $\Phi=40\%$ . We find that the break-up time is shorter for the rock  
116 with  $\Phi=20\%$  than for that with  $\Phi=40\%$  (Extended Data Figure 8), suggesting that fine regolith is  
117 more likely to be produced from the former. This is consistent with the correlation of Figure 1.

118

119 We infer that low-porosity rocks produce more fine regolith than high-porosity rocks by means  
120 of both meteoroid impacts and thermal cracking (Figure 3). This explains the lack of extensive  
121 fine-regolith-covered areas on Bennu<sup>9</sup>, where most rocks are highly porous (ref. 10; Figure 2).

122

123 We argue that the frustration of fine-regolith build-up in the presence of high-porosity rocks  
124 could be a general phenomenon on asteroids.

125

126 Analysis of thermal images acquired by JAXA's Hayabusa2 mission<sup>18,25</sup> indicated that Ryugu's  
127 surface globally has  $\Gamma \approx 225 \pm 45 \text{ Jm}^{-2}\text{K}^{-1}\text{s}^{-0.5}$ , some  $D_R > 50 \text{ m}$  boulders have  $\Gamma_R \approx 115\text{--}160$   
128  $\text{Jm}^{-2}\text{K}^{-1}\text{s}^{-0.5}$ , and a few small boulders have  $\Gamma_R \approx 600\text{--}1,000 \text{ Jm}^{-2}\text{K}^{-1}\text{s}^{-0.5}$ , suggesting that most  
129 rocks on Ryugu have porosities similar to Bennu's ( $\Phi \approx 40\text{--}50\%$ , Figure 2; Methods). For  $\Phi \approx 40\text{--}$   
130  $50\%$ , the correlation of Figure 1 indicates that Ryugu, like Bennu, should have less fine regolith  
131 on the surface than asteroids with lower-porosity rocks.

132

133 Conversely, disk-integrated infrared measurements of the stony asteroid (25143) Itokawa  
134 revealed<sup>17</sup> that its rocks have  $\Gamma_R \approx 900 \text{ Jm}^{-2}\text{K}^{-1}\text{s}^{-0.5}$ , corresponding to  $\Phi = 20 \pm 4\%$  (Methods), which  
135 is lower than most rocks on Bennu and Ryugu (Figure 2). Hence, the correlation of Figure 1  
136 implies that Itokawa's most common rocks produce more fine regolith than Bennu's and Ryugu's.  
137 Spacecraft images show that Itokawa's geopotential lows are smooth terrains covered in

138 centimetre-sized regolith<sup>2</sup>, whereas Bennu's and Ryugu's are not<sup>9,7</sup>. Itokawa's smooth terrains  
139 may have formed via global particle-size sorting induced by surface mass motion<sup>2</sup>. Signatures of  
140 mass motion were also observed on Bennu<sup>26</sup> and Ryugu<sup>7</sup>, but smooth fine-regolith-covered  
141 terrains are lacking<sup>9,7</sup>, suggesting that Bennu's and Ryugu's surface abundances of fine regolith  
142 may be globally lower than Itokawa's. This is consistent with our analysis.

143

144 On small asteroids, fine regolith could be emplaced far from the source rock via electrostatic  
145 lofting<sup>27</sup>, ejection during thermal exfoliation<sup>8</sup>, and/or meteoroid impacts<sup>22</sup>. However, the  
146 robustness of the  $\Gamma_R$ - $\alpha$  correlation rules out an isotropically fine-regolith redistribution from each  
147 local source on Bennu. Further, (i) electrostatic lofting is inefficient at mobilizing centimetre-  
148 sized particles<sup>27</sup>; (ii) exfoliation is only one aspect of thermal cracking, the other being rock  
149 breakup by through-going fracturing without fragment ejection; (iii) the current understanding<sup>22</sup>  
150 is that little mass should be retained by small asteroids from crater ejecta produced by impacts on  
151 low-porosity rocks. However, rocks broken in tightly-clustered pieces were observed on Bennu  
152 (Extended Data Figure 9; refs. 8, 9, and 28), suggesting that regolith is produced by in-situ  
153 fragmentation of large rocks exposed on the surface, similar to what has been observed on the  
154 Moon<sup>29</sup>. Finally, Itokawa may lose more crater ejecta to space than Bennu and Ryugu because  
155 average ejection velocities decrease with increasing target porosity<sup>22</sup>. Despite this, smooth  
156 terrains were only observed on Itokawa<sup>2,7,9</sup>, suggesting that its fine-regolith losses are  
157 compensated by a higher production than Bennu's and Ryugu's.

158

159 The wide range of rock porosities measured on Bennu and Ryugu likely originated on their  
160 parent bodies<sup>25</sup>. We postulate that high-porosity rocks subjected to impacts can be compacted



161 without target disruption<sup>30</sup>. Crushing in high-porosity materials can enhance shear strain and  
162 cause associated frictional heating<sup>31</sup>; this may have assisted lithification of the chondrite  
163 precursors into the lower-porosity carbonaceous breccias that dominate the CM and CI meteorite  
164 collection<sup>14</sup> and were also observed on Bennu<sup>28</sup> and Ryugu<sup>7</sup>.

165

166 1. Veverka, J. et al. The landing of the NEAR-Shoemaker spacecraft on asteroid 433 Eros.  
167 *Nature* **413**, 390–393 (2001).

168 2. Miyamoto, H. et al. Regolith migration and sorting on asteroid Itokawa. *Science* **316**, 1011–  
169 1014 (2007).

170 3. Huang, J. et al. The Ginger-shaped Asteroid 4179 Toutatis: New observations from a  
171 Successful Flyby of Chang'e-2. *Scientific reports* **3**, 3411 (2013).

172 4. Emery, J. et al. Thermal infrared observations and thermophysical characterization of  
173 OSIRIS-REx target asteroid (101955) Bennu. *Icarus* **234**, 17–35 (2014).

174 5. Müller, T. et al. Hayabusa-2 mission target asteroid 162173 Ryugu (1999 JU3): Searching for  
175 the object's spin-axis orientation. *Astronomy & Astrophysics* **599**, A103 (2017).

176 6. Ballouz, R.-L. et al. Bennu's near-Earth lifetime of 1.75 million years inferred from craters  
177 on its boulders. *Nature* **587**, 205–209 (2020).

178 7. Sugita, S. et al. The geomorphology, color, and thermal properties of Ryugu: Implications for  
179 parent-body processes. *Science* **364**, 6437 (2019).

180 8. Molaro, J. L. et al. Thermal fatigue as a driving mechanism for activity on asteroid Bennu.  
181 *Journal of Geophysical Research: Planets* **125**, e2019JE006325 (2020).

182 9. Laretta, D. et al. The unexpected surface of asteroid (101955) Bennu. *Nature* **568**, 55–60  
183 (2019).

- 184 10. Rozitis, B. et al. Asteroid (101955) Bennu's weak boulders and thermally anomalous equator.  
185 *Science Advances* **6**, 41 (2020).
- 186 11. Flynn, G. J. et al. Hypervelocity cratering and disruption of porous pumice targets:  
187 Implications for crater production, catastrophic disruption, and momentum transfer on porous  
188 asteroids. *Planetary and Space Science* **107**, 64–76 (2015).
- 189 12. Housen, K. R., Sweet, W. J. & Holsapple, K. A. Impacts into porous asteroids. *Icarus* **300**,  
190 72–96 (2018).
- 191 13. DeMeo, F., Alexander, C., Walsh, K., Chapman, C. & Binzel, R. The compositional structure  
192 of the asteroid belt. In *Asteroids IV*, 13–41 (2015).
- 193 14. Bischoff, A., Scott, E. R. D., Metzler, K. & Goodrich, C. A. Nature and Origins of Meteoritic  
194 Breccias. In *Meteorites and the Early Solar System II*, 679 (2006).
- 195 15. Christensen, P. R. et al. The OSIRIS-REx thermal emission spectrometer (OTES) instrument.  
196 *Space Science Reviews* **214**, 87 (2018).
- 197 16. Delbo, M., Mueller, M., Emery, J. P., Rozitis, B. & Capria, M. T. Asteroid Thermophysical  
198 Modeling. In *Asteroids IV*, 107–128 (2015).
- 199 17. Cambioni, S., Delbo, M., Ryan, A. J., Furfaro, R. & Asphaug, E. Constraining the thermal  
200 properties of planetary surfaces using machine learning: Application to airless bodies. *Icarus*  
201 **325**, 16–30 (2019).
- 202 18. Shimaki, Y. et al. Thermophysical properties of the surface of asteroid 162173 Ryugu:  
203 Infrared observations and thermal inertia mapping. *Icarus* **348**, 113835 (2020).
- 204 19. Grott, M. et al. Low thermal conductivity boulder with high porosity identified on C-type  
205 asteroid (162173) Ryugu. *Nature Astronomy* **3**, 971–976 (2019).

- 206 20. Opeil, C. P., Britt, D. T., Macke, R. J. & Consolmagno, G. J. The surprising thermal  
207 properties of CM carbonaceous chondrites. *Meteoritics and Planetary Science* **55**, E1–E20  
208 (2020).
- 209 21. Hamilton, V. et al. Evidence for widespread hydrated minerals on asteroid (101955) Bennu.  
210 *Nature Astronomy* **3**, 332–340 (2019).
- 211 22. Michikami, T., Moriguchi, K., Hasegawa, S. & Fujiwara, A. Ejecta velocity distribution for  
212 impact cratering experiments on porous and low strength targets. *Planetary and Space*  
213 *Science* **55**, 70–88 (2007).
- 214 23. Avdellidou, C. et al. Very weak carbonaceous asteroid simulants I: Mechanical properties  
215 and response to hypervelocity impacts. *Icarus* **341**, 113648 (2020).
- 216 24. Delbo, M. et al. Thermal fatigue as the origin of regolith on small asteroids. *Nature* **508**,  
217 233–236 (2014).
- 218 25. Okada, T. et al. Highly porous nature of a primitive asteroid revealed by thermal imaging.  
219 *Nature* **579**, 518–522 (2020).
- 220 26. Jawin, E. et al. Global patterns of recent mass movement on asteroid (101955) Bennu.  
221 *Journal of Geophysical Research: Planets* **125**, e2020JE006475 (2020).
- 222 27. Hsu, H., Wang, X., Carroll, A., Hood, N. & Horanyi, M. Electrostatic removal of fine-  
223 grained regolith on sub-km asteroids. In *AAS/Division for Planetary Sciences Meeting*  
224 *Abstracts* **52**, 402.06 (2020).
- 225 28. Walsh, K. et al. Craters, boulders and regolith of (101955) Bennu indicative of an old and  
226 dynamic surface. *Nature Geoscience* **12**, 242–246 (2019).
- 227 29. Ruesch, O. et al. In situ fragmentation of lunar blocks and implications for impacts and solar-  
228 induced thermal stresses. *Icarus* **336**, 113431 (2020).

229 30. Scott, E. R. D. & Bottke, W. F. Impact histories of angrites, eucrites, and their parent bodies.  
230 *Meteoritics and Planetary Science* **46**, 1878–1887 (2011).

231 31. Bland, P. A. et al. Pressure-temperature evolution of primordial solar system solids during  
232 impact-induced compaction. *Nature Communications* **5**, 5451 (2014).

233

234 **Fig. 1. The thermal inertia of Bennu's rocks is positively correlated with the local surface**  
235 **abundance of fine regolith.** The data points are grey-shaded in terms of  $\Phi$  estimated from  $\Gamma_R$   
236 (Methods). The red points correspond to 13 areas where  $\alpha$  could be overestimated because of the  
237 presence<sup>10</sup> of boulders whose  $\Gamma_R$  could be lower than the threshold value between fine regolith  
238 and rocks (Methods). The plotted solutions have  $\chi^2_r < 3$  as goodness-of-fit (Methods), which is  
239 satisfactory for these types of observations. The error bars correspond to 1 standard deviation  
240 (Supplementary Table 1; Methods) computed on ~670 samples on average.

241

242 **Fig. 2. The porosity of most of Bennu's and Ryugu's rocks is much higher than Itokawa's.**  
243 The porosity values of Bennu's rocks are weighted according to rock abundance ( $1-\alpha$ ) and are  
244 binned using the Freedman-Diaconis rule. The magenta- and green-shaded areas indicate the  
245 estimated surface-averaged ranges of rock porosity on asteroids Ryugu<sup>18,19</sup> and Itokawa<sup>17</sup>,  
246 respectively. About 70% of the rocks on Bennu are as porous as Ryugu's, while only ~5% of  
247 Bennu's rocks have porosity similar to Itokawa's.

248

249 **Fig. 3. Fine-regolith production is frustrated in the presence of high-porosity rocks.** On  
250 asteroids, rocks with higher porosity are compacted by meteoroid impacts rather than

251 excavated<sup>12</sup>. Thermal stresses in a more porous rock are weaker in magnitude than in a denser  
252 rock<sup>8</sup>, implying that the former could be less prone to producing fine regolith than the latter.

253

## 254 **Methods**

### 255 **Two-component thermophysical modelling**

256 The global mosaic of images<sup>32</sup> acquired by the PolyCam imager of the OSIRIS-REx Camera  
257 Suite (OCAMS<sup>33</sup>) with resolution 5 cm pixel<sup>-1</sup> shows that Bennu's surface is composed of a  
258 mixture of rocks and, to a lesser extent, unresolved materials<sup>28,34</sup>. The latter may include fine  
259 regolith with particle size  $D_P < l_s = [\kappa / (c_p \rho) P / \pi]^{1/2}$ , where  $P$  is the asteroid's rotation period. These  
260 observations motivate us to determine the surface abundance of fine regolith ( $\alpha$ ) with respect to  
261 the surface abundance ( $1-\alpha$ ) of rocks with size  $D_R > l_s$ .

262

263 To this end, we select 122 quasi-randomly-distributed regions (OTES spots; Extended Data  
264 Figure 1) and use a machine learning two-component thermophysical model<sup>17</sup> to simultaneously  
265 fit infrared radiance spectra emitted from the asteroid at the local times 3:20 a.m. and 3:00 p.m.  
266 to derive the surface properties ( $\theta$ ,  $\Gamma_P$ ,  $\Gamma_R$ ,  $\alpha$ ). The 3:20 a.m. station is the coldest and farthest in  
267 time from sunrise, when the brightness temperature of smaller rocks may approach that of colder  
268 fine regolith; the 3:00 p.m. station is diametrically opposed to the 3:20 a.m. station, close to the  
269 time of peak surface temperature, and not at the crossing point between diurnal temperature  
270 curves for different  $\Gamma$  values, where the thermophysical solution could be degenerate (Figure 2 in  
271 ref. 10). Furthermore, the spots on the surface for the 3:00 p.m. and 3:20 a.m. stations are well  
272 aligned, which minimises mismodelling. Modelling 122 areas instead of the full surface makes  
273 the machine-learning analysis computationally feasible while still investigating a representative

274 sample of Bennu's surface. Among the 122 spots, 100 are randomly selected and 22 were  
275 manually added to be centred as much as possible on distinct, interesting and representative  
276 geological features such as (i) the designated sampling sites; (ii) large boulders filling the OTES  
277 spot; (iii) regions with high boulder abundance; and (iv) areas with low boulder abundance.

278

279 For each area and time of day, we use the OTES' acquisition mid-observation time and boresight  
280 to calculate the longitude and latitude of the OTES spot's centre and diameter projected on  
281 Bennu's surface. The surface is modelled using the 6-m-resolution SPC/OLA v34 shape model  
282 composed of triangular facets and derived from a combination of stereophotoclinometry and  
283 laser ranging<sup>35</sup>; its pole orientation<sup>9,10</sup> is J2000 ecliptic longitude  $69.92^\circ$  and latitude  $-83.45^\circ$ . The  
284 observation geometry for each spot and time of the day (i.e., ephemerides of the OSIRIS-REx  
285 spacecraft and the asteroid) is computed using the `spiceypy` Python-wrapper for the SPICE  
286 Toolkit. The kernel files are directly sourced from the SPICE kernels produced by the mission.  
287 For each observation geometry, we build the local set of facets of Bennu's topographic model by  
288 drawing concentric circles (with radius ranging between 0 and that of the OTES spot and centred  
289 at the spot's centre) and by drawing radial vectors with origin in the spot's centre and length  
290 between 0 and the spot's radius. Since we limited our survey to latitudes between  $\pm 60^\circ$ , each  
291 OTES spot is well-approximated by a circle with a diameter of 40 m that corresponds to the  
292 instrument footprint. All the unique facets that lie at the intersection between a circle and a radial  
293 vector belong to the local set.

294

295 For each OTES spot and for each observation time, we set up thermophysical simulations using a  
296 well-defined model<sup>16</sup> that uses the aforementioned observation geometry, asteroid illumination,

297 asteroid spin state, and local sets of facets of Bennu's shape model as input. We create lookup  
298 tables of simulations where  $\Gamma$  varies between 25 and 2,500  $\text{Jm}^{-2}\text{K}^{-1}\text{s}^{-0.5}$  (the upper limit  
299 corresponding to low-porosity meteorites<sup>20</sup>) with step 25 and  $\theta$  is modelled using hemispherical  
300 craters with surface crater density ( $f_c$ ) ranging between 0 and 0.99 with step 0.14 (as such,  
301  $\theta=49f_c^{1/2}$  represents roughness RMS slope<sup>10</sup>). We assume a fixed value of Bolometric Bond's  
302 albedo equal to 0.02 and infrared emissivity  $\epsilon=0.95$  (as previously done<sup>10</sup>). The shape model's  
303 rotation and daily temperature cycle are simulated for 15 Julian days until the temperature cycle  
304 converges to a stable cycle. After this, we output the simulated radiance at the epoch of the  
305 OTES observation between 6 and 50  $\mu\text{m}$ , where the OTES noise equivalent spectral radiance  
306 (NESR, which represents the  $1\sigma$  variation in calibrated radiance) is the lowest<sup>15</sup>.

307

308 Next, for each OTES spot and for each observation time, we use the aforementioned look-up  
309 table of thermophysical simulations to train a neural network that generalizes the prediction of  
310 the radiance as a function of  $\Gamma$  and  $\theta$ . The step of training the neural networks and using them in  
311 the fitting routine makes the exploration of the large, multi-dimensional parameter space of  
312 solutions computationally possible. This approach is particularly potent for the case of Bennu as  
313 both day-side and night-side data are available with a wide spectral wavelength range<sup>15,17</sup>. The  
314 70% of model radiances is used for training via stochastic gradient descent and a neural network  
315 architecture with 1 hidden layer of 10 neurons, which is the optimal scheme<sup>17</sup>. Another 15% of  
316 the dataset is used to protect the networks against overfitting the training data. We use the last  
317 15% of the dataset to assess the networks' performance on unseen data in terms of mean squared  
318 error between the predicted and target radiances. The networks generalise well the prediction of  
319 the model radiances at testing: the average errors are equal to 0.2% and 0.9% of the radiance

320 peak value for  $\Gamma=350 \text{ Jm}^{-2}\text{K}^{-1}\text{s}^{-0.5}$  and  $\theta=43^\circ$  (which are the average surface thermophysical  
 321 properties of Bennu<sup>10</sup>) for the 3:20 a.m. and 3:00 p.m. observations, respectively; the correlation  
 322 coefficient between predicted and target radiances is  $>0.99$ .

323

324 Next, we use the networks to simulate the radiance  $L_{\text{regolith}}$  emitted by fine regolith of thermal  
 325 inertia  $\Gamma_P$  and that emitted by rocks of thermal inertia  $\Gamma_R$  ( $L_{\text{rock}}$ ), and linearly combine them to  
 326 model the radiance  $L_{\text{model}}$  emitted by a mixture of fine regolith and rocks:

$$327 \quad L_{\text{model}}[f_s, \theta, \Gamma_P, \Gamma_R, \alpha] = f_s \times (\alpha L_{\text{regolith}}[\Gamma_P, \theta] + (1-\alpha) L_{\text{rock}}[\Gamma_R, \theta]), \quad (1)$$

328 where  $f_s$  is an optional scaling factor which is adjusted during the model fit to account for small  
 329 modelling errors caused by (unknown) inaccuracies in the topographic model and/or potential  
 330 deficiencies of the surface roughness<sup>10</sup>.  $\Gamma_P$  can assume values between  $25 \text{ Jm}^{-2}\text{K}^{-1}\text{s}^{-0.5}$  and  $\Gamma_c$ ,  
 331 and  $\Gamma_R$  between  $\Gamma_c$  and  $2,500 \text{ Jm}^{-2}\text{K}^{-1}\text{s}^{-0.5}$ , where  $\Gamma_c$  is the thermal inertia “cut-off” value of  
 332 regolith whose particles have  $D_p=1_s$ . It is computed as follows. For each area, we postulate that  
 333 fine regolith is produced by the comminution of local rocks by meteoroid impacts<sup>36</sup> and thermal  
 334 cracking<sup>24</sup>. This implies that fine regolith particles inherit the thermal conductivity  $\kappa$ , grain  
 335 density  $\rho_s$ , and porosity  $\Phi$  of the rock.  $\kappa$  is obtained using the fit of meteorite values<sup>37</sup>

$$336 \quad \kappa(\Phi) = \frac{\Gamma_R^2}{c_p \rho_s (1-\Phi)} = \frac{0.11(1-\Phi)}{\Phi} \quad (2)$$

337 where  $\rho_s=2920 \text{ kg m}^{-3}$  for CM meteorites<sup>38</sup> and  $c_p$  is the heat capacity for the meteorite CM2  
 338 Cold Bokkeveld<sup>20</sup> at the OTES spot's mean diurnal temperature<sup>10</sup>. Although alternative  
 339 relationships of thermal conductivity versus rock porosity are available<sup>19</sup>, Eq. 2 is the model that  
 340 also fits well more recent results for super-weak CM-like materials<sup>23</sup>. Since  $\Gamma_R$  is a fitted  
 341 parameter, the procedure for determining  $\Gamma_c$  is necessarily iterative; we initialise the iteration  
 342 assuming  $\Gamma_R$  equal to the single-component thermal inertia derived by previous studies<sup>10</sup>. We use



343 a standard<sup>39</sup> regolith model to calculate particulate regolith bulk thermal conductivity ( $\kappa_p$ ) as a  
 344 function of particle diameter  $D_p$ . These values are compared to respective values of  $l_s=l_s(\kappa_p)$  to  
 345 find the value of  $\kappa_p$  where  $D_p=l_s$ . This value of  $\kappa_p$  is combined with  $c_p$  and  $\rho=\rho_s\times(1-\Phi)\times(1-\phi)$  to  
 346 calculate  $\Gamma_c$  ( $\phi$  is the regolith macroporosity, that is, the volume of voids between particles). We  
 347 use published<sup>10</sup> model parameters and assume:  $\zeta=0.68+7.6\times 10^{-5}D_p^{-1}$  as the ratio of the effective  
 348 distance of radiative heat transfer in the voids between particles to the void geometric  
 349 size<sup>39,40</sup>,  $\xi=0.12$  as the degree of reduction of the thermal conductance at the contacts between  
 350 particles owing to the microscopic surface roughness<sup>39</sup>, infrared emissivity<sup>10</sup>  $\varepsilon=0.95$ , and regolith  
 351 macroporosity  $\phi=40\%$ . The latter is an often-used value and represents a loose random packing  
 352 of spherical particles<sup>41</sup>. We take into account thermal gradients within individual regolith  
 353 particles using the non-isothermal correction factor<sup>41</sup> as in previous work<sup>10</sup>.

354

355 For a given  $\Gamma_c$  and assuming  $\theta$  from published<sup>10</sup> results, we explore all possible combinations of  
 356 the free parameters  $x=(f_s^{3:00 \text{ p.m.}}, f_s^{3:20 \text{ a.m.}}, \Gamma_p, \Gamma_R, \alpha)$  to identify the best-fit radiance that  
 357 minimises the error function:

$$358 \chi_r^2 = \frac{1}{\text{obs-df}} \left( \sum_{\lambda=6}^{50 \mu\text{m}} \frac{[L_{\text{model}}^{3:00 \text{ p.m.}}(x, \lambda) - L_{\text{OTES}}^{3:00 \text{ p.m.}}(\lambda)]^2}{\sigma^2} + \sum_{\lambda=6}^{50 \mu\text{m}} \frac{[L_{\text{model}}^{3:20 \text{ a.m.}}(x, \lambda) - L_{\text{OTES}}^{3:20 \text{ a.m.}}(\lambda)]^2}{\sigma^2} \right) \quad (3)$$

359 where  $L_{\text{OTES}}$  is the observed radiance re-sampled with step  $1 \mu\text{m}$ ,  $\sigma$  is the error measurement  
 360 equal to 3 times the OTES' pre-flight<sup>15</sup> 772 Hz NESR, obs is the number of observations and  
 361  $\text{df}=5$  is the number of parameters to fit. The uncertainties of the free parameters are computed as  
 362 the standard deviation of the set of solutions whose  $\chi_r^2 < \min(\chi_r^2) + [2/(\text{obs}-\text{df})]^{1/2}$ , as typically  
 363 done in thermophysical modelling<sup>42</sup>. Upon completion of the fitting, the best-fit  $\Gamma_R$  is used to  
 364 update the value of  $\Gamma_c$ , which is in turn used to re-compute the best-fit  $(f_s^{3:00 \text{ p.m.}}, f_s^{3:20 \text{ a.m.}}, \Gamma_p, \Gamma_R,$   
 365  $\alpha)$ . This loop is repeated until  $|\Gamma_R^i - \Gamma_R^{i-1}| < \sigma_R^{i-1}$ , where (i) indicates the present iteration and  $\sigma_R^{i-1}$

366 is the standard deviation of  $\Gamma_R$  obtained at the iteration (i-1)-th. Convergence is typically reached  
367 in four iterations. Once the analysis is completed, we add a cautionary 10% relative error to the  
368 uncertainties because previous studies<sup>10</sup> found that the thermophysical solution obtained by  
369 fitting the 3:00 p.m. and 3:20 a.m. data is within 10% of the value obtained by including  
370 additional OTES data acquired at other times of the day.

371  
372 Finally, we reject 25 spots where the best-fit solutions have  $\chi_r^2 > 10$  and/or for which no  
373 convergence is found for  $\Gamma_R \leq 2490 \text{ Jm}^{-2}\text{K}^{-1}\text{s}^{-0.5}$ . We carry the analysis and tests reported below  
374 on the remaining 97 spots (Supplementary Table 1).

375

### 376 **Tests of the robustness of the results**

377 We test whether the measured  $\alpha$ -values are consistent with the surface abundance of unresolved  
378 materials seen in PolyCam<sup>33</sup> images. We do this test for the spots 609505286:610098718 and  
379 609504794:610100730 centred at Osprey and at Nightingale, for which Burke et al. (ref. 43)  
380 performed rock mapping down to  $D_p = 2 \text{ cm} \lesssim l_s$  (results are in Extended Data Figure 2). We note  
381 that the OTES spots have areas at least 38 and 20 times larger than those within which rocks  
382 were visually mapped at Osprey and Nightingale, respectively.

383

384 We also test that the value of  $\alpha$  is always smaller or equal than the surface area of unresolved  
385 materials that we can visually see, at coarser spatial resolution than at Osprey and Nightingale,  
386 within the entire OTES spot. We choose the spots 609493058:610103962 and  
387 609487186:610098206 where we perform rock mapping as similarly done in ref. 43 on PolyCam  
388 images at a spatial resolution of  $5 \text{ cm pixel}^{-1}$  (thus,  $> l_s$ ). The area of each rock is computed as

389 that of a circle with diameter equal to the rock's longest dimension. One minus the sum of rocks'  
390 areas divided by the area of the OTES spot is provided as % of unresolved material in Extended  
391 Data Figure 3, along with the value of  $\alpha$ . We also check that the size distributions of the mapped  
392 rocks are consistent with that globally mapped on Bennu<sup>34</sup>, meaning that the two sites are  
393 representative of average Bennu.

394

395 We use the two-sided Spearman test to reject the null hypothesis that a random distribution of  
396  $\Gamma_R$ - and  $\alpha$ -values could produce the observed correlation of Figure 1 (Extended Data Figure 4).  
397 To take into account uncertainties in the values of  $\Gamma_R$  and  $\alpha$ , we perform the Spearman test  
398 10,000 times, where at each trial we vary  $\Gamma_R$  and  $\alpha$  within their uncertainties. We draw the  
399 samples from Gaussian distributions with mean and standard deviation equal to the nominal  
400 value and uncertainties of  $\Gamma_R$  and  $\alpha$ .

401

402 We repeat the Spearman test after we reject 13 areas where large dark boulders fill the OTES  
403 spot (red data points in Figure 1). Bennu's dark boulders tend to have low  $\Gamma_R$  values<sup>10,34</sup>, although  
404 the lower limit of  $\Gamma_R$  is unknown because only one boulder was spatially resolved by the OTES  
405 instrument<sup>10</sup>. If the boulders'  $\Gamma_R < \Gamma_c$ , their surface abundance would erroneously contribute to the  
406 surface abundance of fine regolith  $\alpha$  instead of being counted as rocks, with the caveat that fine  
407 regolith could be present on top of the boulders<sup>10</sup>.

408

409 We investigate whether the  $\Gamma_R$ - $\alpha$  correlation is sensitive to the assumed value of regolith  
410 macroporosity  $\phi$  (Extended Data Figure 5). We repeat the thermophysical modelling of all OTES  
411 spots for a low-end value of  $\phi=15\%$ , which is an estimate for the whole asteroid based on a

412 boulder size-frequency distribution analysis<sup>44</sup>, and a high-end value of  $\phi=60\%$ , which is a  
413 compromise reduction from much higher values used in previous studies (e.g.  $\phi=80\%$ , ref. 45,  
414 which we consider unlikely for a polydisperse size-frequency-distribution). We perform a  $3\sigma$  test  
415 on the solutions to identify those areas where  $(\Gamma_P, \Gamma_R, \alpha)$  for  $\phi=15\%$  and  $\phi=60\%$  are statistically  
416 distinct from those for  $\phi=40\%$ . This test is done considering only those spots where a converged  
417 solution is found for both macroporosities: 93 spots ( $\phi=40\%$  versus  $\phi=15\%$ ) and 90 spots  
418 ( $\phi=40\%$  versus  $\phi=60\%$ ). We repeat the Spearman test to assess the robustness of the correlation  
419 against removing the areas with statistically distinct solutions from the dataset.

420

421 We investigate whether the  $\Gamma_R$ - $\alpha$  correlation may be an artefact due to the assumption of linear  
422 mixing between the radiances emitted by fine regolith and rocks (Eq. 1). We simulate synthetic  
423 radiances emitted from a single triangular facet with zero roughness and thermal inertia values  
424 following the step function  $\Gamma(\alpha)$ :  $\Gamma \leq \Gamma_c = 100 \text{ Jm}^{-2}\text{K}^{-1}\text{s}^{-0.5}$  for  $\alpha=100\%$  and  $100 < \Gamma < 2,500$   
425  $\text{Jm}^{-2}\text{K}^{-1}\text{s}^{-0.5}$  for  $\alpha=0\%$ . We simulate the observation of these model radiances by OTES and fit  
426 them using our thermophysical model to see whether we retrieve the modelled step function or a  
427 correlation similar to that of Figure 1 is instead obtained (Extended Data Figure 6).

428

429 Finally, it has been suggested<sup>10,34,46</sup> that dark boulders (normal reflectance 0.034–0.049) are more  
430 abundant, can reach higher diameters, and have lower thermal inertia than the bright boulders  
431 (normal reflectance 0.049–0.074). These boulder properties could mimic the  $\Gamma_R$ - $\alpha$  correlation of  
432 Figure 1 if  $\alpha$  was also negatively correlated with the area of the largest boulder in the OTES spot.  
433 Using the boulder database of ref. 46 we plot the  $\alpha$ -value as a function of the size of the largest

434 boulder and perform the Spearman test to investigate whether these quantities are correlated  
435 (results are in Extended Data Figure 7).

436

### 437 **Interpretation of the results**

438 For each OTES spot, we compute the rock porosity  $\Phi$  from the best-fit  $\Gamma_R$  by means of Eq. 2,  
439 assuming  $\rho_s$  and  $c_p$  as for the computation of  $\Gamma_c$ . The range of  $\Phi$ -values for Ryugu in Figure 2  
440 corresponds to that estimated<sup>19</sup> using Eq. 2 for the boulder observed by the MASCOT infrared  
441 radiometer, whose type is typical<sup>25</sup> on Ryugu. We use Eq. 2 also to compute  $\Phi$  of the rocks on  
442 Itokawa from the published<sup>17</sup> value of  $\Gamma_R=894\pm 122 \text{ Jm}^{-2}\text{K}^{-1}\text{s}^{-0.5}$  assuming the composition of LL  
443 chondrites, which is that of the samples returned from Itokawa<sup>47</sup>:  $\rho_s=3220 \text{ kg m}^{-3}$  and  $c_p=682$   
444  $\text{Jkg}^{-1}\text{K}^{-1}$ . We compute the uncertainty of Itokawa's  $\Phi$  as  $\sigma(\Phi)=\partial\Phi/\partial\Gamma_R\times\sigma(\Gamma_R)$ , where  $\sigma(\Gamma_R)$  is the  
445 uncertainty of Itokawa's  $\Gamma_R$  from ref. 17.

446

447 Next, we use this information to estimate the time to break a rock of diameter  $D_R$  by thermal  
448 fatigue ( $t_B$ ). We use known models<sup>24,48</sup> to simulate a bed of polydispersed spherical rocks, whose  
449 surface is exposed to cyclic temperature variations driven by sunlight; on each rock, an initially  
450 sub-mm-sized fracture placed on the surface propagates downward in the rock (i.e., towards the  
451 centre of the asteroid), until its size,  $a$ , becomes equal to  $D_R$ , which is the condition for rock  
452 break-up. The time to fracture,  $t_B$ , can be calculated from the fracture growth rate  $da/dN$ , which  
453 is typically approximated<sup>24</sup> using Paris' law:  $da/dN=C[\Delta K_I(a)]^n$ , where  $N$  is the number of  
454 temperature cycles,  $C$  and  $n$  have values determined from experiments or analogy with asteroid  
455 simulant materials<sup>24</sup>, and  $\Delta K_I$  is the maximum variation of the stress intensity factor ( $K_I$ ) for  
456 fracture opening mode. The latter is related to the stress  $\tau$  experienced by the material during a

457 temperature cycle.  $\Delta K_I \propto \tau \propto \Delta T$ , which is the maximum diurnal temperature excursion<sup>24</sup>.  
 458 Moreover, from Eq. 23 of ref. 48 we can write that  $t_B/P = \Lambda' (D_R/l_s)^{1/m}$ , where P is the asteroid  
 459 rotation period;  $m=1/(1-n)$  for  $D_R/l_s \leq 1$  and  $m=1/(n-1)$  for  $D_R/l_s > 1$ . Hence:

$$460 \quad \frac{t_B}{P} = N = \Lambda'' \left( \frac{D_R}{l_s} \right)^{\frac{1}{m}} (\Delta T)^{-n} \quad (4)$$

461 Given N cycles required to break a rock with a certain  $D_R/l_s$ , material properties, geometry and  
 462  $\Delta T$ , we derive the value of  $\Lambda''$  and use Eq. 4 to predict  $t_B$  for rocks of different sizes at different  
 463  $\Delta T$ . First, we calculate  $l_s$  to be 6.4 and 8.6 cm for the carbonaceous and the ordinary chondrite of  
 464 ref. 24 for which, at  $D_R=l_s$ , their Figure 1 gives  $t=3.5 \times 10^3$  and  $6.3 \times 10^3$  years, respectively,  
 465 corresponding to  $N=1.4 \times 10^6$  and  $N=14 \times 10^6$  cycles, given their  $P=6$  hours. We take  $\Delta T$  from their  
 466 Extended Data Figure 2. Next, we use Eq. 4 to derive  $t_B$  as a function of  $D_R$  for values of  $l_s$ , P  
 467 and  $\Delta T$  that are more appropriate for Bennu, Ryugu and Itokawa than those of ref. 24. From the  
 468 latter reference we take the carbonaceous chondrite properties, but we use  $\Gamma_R=500 \text{ Jm}^{-2}\text{K}^{-1}\text{s}^{-0.5}$ ,  
 469 which is more appropriate for the high- $\Phi$ , low- $\Gamma_R$  rocks that dominate Bennu's and Ryugu's  
 470 surfaces (Figure 2 and ref. 18, 19, 25, respectively). For the ordinary chondrite, we use  $\Gamma_R=900$   
 471  $\text{Jm}^{-2}\text{K}^{-1}\text{s}^{-0.5}$ , as the latter value was derived from astronomical observations<sup>17</sup> of Itokawa, and we  
 472 assume that these parameters could also represent low- $\Phi$ , high- $\Gamma_R$  rocks which may be present  
 473 on Bennu's and Ryugu's surface, but in lower abundance than the high- $\Phi$ , low- $\Gamma_R$  rocks. The  
 474 rotation periods are  $P=4.296$ , 7.63, and 12.1 hours for Bennu<sup>49</sup>, Ryugu<sup>50</sup>, and Itokawa<sup>51</sup>,  
 475 respectively. However, since these rotation periods could have been different<sup>49</sup> in the past, due to  
 476 the Yarkovsky–O'Keefe–Radzievskii–Paddack (YORP) effect, we consider generic low- $\Gamma_R$ ,  
 477 high- $\Phi$  and high- $\Gamma_R$ , low- $\Phi$  cases with  $P=4.296$  and 12.1 hours for a total of four cases. For each  
 478 of them we calculate their  $l_s$ -values and run a thermophysical model to determine, at 1.2 au of

479 heliocentric distance, the values of  $\Delta T$ . Finally, using Eq. 4 we produce the Extended Data  
480 Figure 8.

481

#### 482 **Data Availability**

483 Raw through calibrated OTES<sup>52</sup> and OCAMS<sup>53</sup> data are available via the Planetary Data System  
484 at <https://sbn.psi.edu/pds/resource/orex/>. The SPC/OLA v34 shape model is available via the  
485 Small Body Mapping Tool at <http://sbmt.jhuapl.edu/>. The IDs of the OTES observations used in  
486 this study and the best-fit solutions for the thermophysical model are in Supplementary Table 1.  
487 The boulder size, location and reflectance used to test the robustness of the results are in refs. 34  
488 and 46.

489

#### 490 **Code Availability**

491 The thermophysical analysis reported here uses a custom code based on the Thermophysical  
492 Model of ref. 16, available at  
493 [www.oca.eu/images/LAGRANGE/pages\\_perso/delbo/thermops.tar.gz](http://www.oca.eu/images/LAGRANGE/pages_perso/delbo/thermops.tar.gz). The code to compute the  
494 geometry of the OTES acquisitions and boresight is available in Zenodo with the identifier  
495 10.5281/zenodo.4781752 (ref. 54). The code to compute the values of  $\Gamma_c$  for the thermophysical  
496 analysis is available in Zenodo with the identifier 10.5281/zenodo.4763783 (ref. 55). The rock  
497 mapping of Extended Data Figure 3 was performed using the SAOImageDS9 software available  
498 at [cfa.harvard.edu/saoimageds9](http://cfa.harvard.edu/saoimageds9). Other codes that support the findings of this study are available  
499 in Zenodo with the identifier 10.5281/zenodo.4771035 (ref. 56).

500

- 501 32. Bennett, C. et al. A high-resolution global basemap of (101955) Bennu. *Icarus* **357**, 113690  
502 (2020).
- 503 33. Rizk, B. et al. OCAMS: the OSIRIS-REx camera suite. *Space Science Reviews* **214**, 26  
504 (2018).
- 505 34. DellaGiustina, D. et al. Properties of rubble-pile asteroid (101955) Bennu from OSIRIS-REx  
506 imaging and thermal analysis. *Nature Astronomy* **3**, 341–351 (2019).
- 507 35. Barnouin, O. et al. Digital terrain mapping by the OSIRIS-REx mission. *Planetary and Space*  
508 *Science* **180**, 104764 (2020).
- 509 36. Horz, F. & Cintala, M. Impact Experiments Related to the Evolution of Planetary Regoliths.  
510 *Meteoritics and Planetary Science Supplement* **31**, A65 (1996).
- 511 37. Flynn, G. J., Consolmagno, G. J., Brown, P. & Macke, R. J. Physical properties of the stone  
512 meteorites: Implications for the properties of their parent bodies. *Chemie der Erde* **78**, 269–  
513 298 (2018).
- 514 38. Macke, R. J., Consolmagno, G. J. & Britt, D. T. Density, porosity, and magnetic  
515 susceptibility of carbonaceous chondrites. *Meteoritics & Planetary Science* **46**, 1842–1862  
516 (2011).
- 517 39. Sakatani, N., Ogawa, K., Arakawa, M. & Tanaka, S. Thermal conductivity of lunar regolith  
518 simulant JSC-1A under vacuum. *Icarus* **309**, 13–24 (2018).
- 519 40. Wada, K. et al. Asteroid Ryugu before the Hayabusa2 encounter. *Progress in Earth and*  
520 *Planetary Science* **5**, 82 (2018).
- 521 41. Ryan, A. J., Pino Muñoz, D., Bernacki, M. & Delbo, M. Full-Field Modeling of Heat  
522 Transfer in Asteroid Regolith: Radiative Thermal Conductivity of Polydisperse Particulates.  
523 *Journal of Geophysical Research: Planets* **125**, e2019JE006100 (2020).



- 524 42. Hanuš, J., Delbo, M., Ďurech, J. & Ali-Lagoa, V. Thermophysical modeling of main-belt  
525 asteroids from WISE thermal data. *Icarus* **309**, 297–337 (2018).
- 526 43. Burke, K. N. et al. Particle Size-Frequency Distributions of the OSIRIS-REx Candidate  
527 Sample Sites on Asteroid (101955) Bennu. *Remote Sensing* **13**, 1315 (2021).
- 528 44. Biele, J. et al. Macroporosity and Grain Density of Rubble Pile Asteroid (101955) Bennu. In  
529 *AGU Fall Meeting 2020* **1**, P037–04 (2020).
- 530 45. Gundlach, B. & Blum, J. A new method to determine the grain size of planetary regolith.  
531 *Icarus* **223**, 479–492 (2013).
- 532 46. DellaGiustina, D. N. et al. Variations in color and reflectance on the surface of asteroid  
533 (101955) Bennu. *Science* **370**, eabc3660 (2020).
- 534 47. Nakamura, T. et al. Itokawa dust particles: a direct link between S-type asteroids and  
535 ordinary chondrites. *Science* **333**, 1113–1116 (2011).
- 536 48. El Mir, C., Ramesh, K. T. & Delbo, M. The efficiency of thermal fatigue in regolith  
537 generation on small airless bodies. *Icarus* **333**, 356–370 (2019).
- 538 49. Hergenrother, C. W. et al. The operational environment and rotational acceleration of  
539 asteroid (101955) Bennu from OSIRIS-REx observations. *Nature Communications* **10**,  
540 1291–10 (2019).
- 541 50. Watanabe, S. et al. Hayabusa2 arrives at the carbonaceous asteroid 162173 Ryugu—A  
542 spinning top-shaped rubble pile. *Science* **364**, 268–272 (2019).
- 543 51. Demura, H. et al. Pole and Global Shape of 25143 Itokawa. *Science* **312**, 1347–1349 (2006).
- 544 52. Christensen, P., Hamilton, V., Anwar, S., Mehall, G. & Lauretta, D. Origins, Spectral  
545 Interpretation, Resource Identification, Security, Regolith Explorer (OSIRIS-REx): OSIRIS-

- 546 REx Thermal Emission Spectrometer Bundle (2019). NASA Planetary Data System,  
547 urn:nasa:pds:orex.otes.
- 548 53. Rizk, B., Golish, D., DellaGiustina, D. & Lauretta, D. Origins, Spectral Interpretation,  
549 Resource Identification, Security, Regolith Explorer (OSIRIS-REx): OSIRIS-REx Camera  
550 Suite (OCAMS) Bundle (2019). NASA Planetary Data System, urn:nasa:pds:orex.ocams.
- 551 54. Deshapriya, J. D. P. OTES geoWriter. Zenodo, <https://doi.org/10.5281/zenodo.4781752>  
552 (2021).
- 553 55. Ryan, A. Regolith heat transfer code for manuscript “Rock porosity drives regolith buildup  
554 on carbon-rich versus stony asteroids”. Zenodo, <http://doi.org/10.5281/zenodo.4763783>  
555 (2021).
- 556 56. Cambioni, S., Delbo, M. & Poggiali, G. Codes for two-component thermophysical analysis  
557 of asteroid (101955) Bennu. Zenodo, <http://doi.org/10.5281/zenodo.4771035> (2021)

558

## 559 **Acknowledgments**

560 This material is based upon work supported by NASA under contract NNM10AA11C issued  
561 through the New Frontiers Program. We are grateful to the entire OSIRIS-REx team for making  
562 the encounter with Bennu possible, to C. Wolner and F. Murphy for editorial help, and to the  
563 OPAL infrastructure of the Observatoire de la Côte d'Azur (CRIMSON) for providing  
564 computational resources and support. S.C. thanks the University of Arizona for supporting this  
565 study. M.D., C.A., J.D.P.D and A.B. acknowledge the French space agency CNES. C.A. and  
566 M.D. acknowledge support from ANR “ORIGINS” (ANR-18-CE31-0014). C.A. was supported  
567 by the French National Research Agency under the project “Investissements d'Avenir”  
568 UCAJEDI ANR-15-IDEX-01. G.P. and J.R.B. were supported by Italian Space Agency grant

569 agreement INAF/ASI n. 2017-37-H.0. B.R. acknowledges financial support from the UK Science  
570 and Technology Facilities Council (STFC). E.A.C. thanks CSA, NSERC, CFI, MRIF and  
571 UWinnipeg for supporting this study.

572

### 573 **Author Contribution**

574 S.C. led the project, the interpretation of the results and manuscript development, and performed  
575 the thermophysical simulations and data analysis. M.D. provided the thermophysical software,  
576 performed the thermal cracking calculations and contributed to the interpretation of the results  
577 and to the development of the manuscript. G.P. developed the pipeline to retrieve OTES detailed  
578 survey data and performed rock mapping in PolyCam images. C.A. curated the discussion on  
579 meteoroid bombardment and contributed to the writing of the manuscript. A.J.R. contributed  
580 with the code to convert thermal inertia values in fine regolith particle size and developed the  
581 iterative approach to determine the cut-off value of thermal inertia together with S.C. J.D.P.D.  
582 contributed by extracting the observation geometry of the spacecraft and Bennu from mission  
583 kernels. R.-L.B. contributed by proposing important tests of the robustness of the results. E.A,  
584 W.F.B. and J.R.B. contributed to the interpretation of the data and the writing of the manuscript.  
585 D.N.D., K.N.B., C.A.B. and K.J.W. contributed by providing support in the interpretation of  
586 spacecraft imagery. J.P.E. and B.R. contributed to the data interpretation during the OSIRIS-REx  
587 Thermal Analysis Working Group meetings, and to design of the observations and data  
588 acquisition. M.A.B. and E.C. contributed to the interpretation of the results. D.S.L. made this  
589 study possible as the PI of the OSIRIS-REx mission and contributed to the discussion of the  
590 results.

591

592 **Author information**

593 Supplementary Information is available for this paper. Reprints and permissions information is  
594 available at [www.nature.com/reprints](http://www.nature.com/reprints). The authors declare no competing interests.  
595 Correspondence and requests for materials should be addressed to Saverio Cambioni  
596 ([saveriocambioni@email.arizona.edu](mailto:saveriocambioni@email.arizona.edu), [saverio@caltech.edu](mailto:saverio@caltech.edu)).

597

598 **Extended Data Fig. 1. The thermal inertia of Bennu's rocks and the surface abundance of**

599 **fine regolith were measured in 122 quasi-randomly–distributed regions.** a, OTES spots on

600 Bennu plotted on the global basemap of Bennu<sup>32</sup> as function of longitude and latitude (red: 3:00

601 p.m. station, or EQ1; blue: 3:20 a.m. station, or EQ2). b, comparison between modelled and

602 observed radiance for one of the 122 areas (ID: 609491396:610102222). c, comparison between

603 the emissivity of Bennu and the residuals of the analysis for the spots 609491396:610102222;

604 the residual curves closely resemble Bennu's emissivity, which is not modelled by our

605 thermophysical model. The error bars correspond to 3 times the Noise Equivalent Spectral

606 Radiance of the OTES instrument<sup>15</sup>.

607

608 **Extended Data Fig. 2. There is less fine regolith at the OSIRIS-REx's backup sampling site**

609 **Osprey than at the primary sampling site Nightingale.** Blue and yellow pixels represent areas

610 where no particles bigger than 2 cm,  $\sim 1$ s, were mapped by ref. 43. The value  $D_p \approx 1_s$  is the upper

611 limit for the sizes of fine regolith detected by our thermophysical model. There are less blue and

612 yellow pixels at Osprey (image resolution: 0.3 cm pixel<sup>-1</sup>, panels a, b) than at Nightingale (image

613 resolution: 0.4 cm pixel<sup>-1</sup>, panels c, d), implying that Osprey has less unresolved material than

614 Nightingale. Consistently and independently, our thermophysical model indicates

615  $\alpha_{\text{Osprey}} < \alpha_{\text{Nightingale}}$  (Supplementary Table 1, spots 609505286:610098718 and  
616 609504794:610100730, respectively).

617

618 **Extended Data Fig. 3. The fine regolith abundance derived from OTES data is lower than**  
619 **the areas of unresolved material measured in Bennu's images.** Our visual mapping and size  
620 measurement of rocks within two OTES spots: a, OTES spots 609493058:610103962; b, OTES  
621 spots 609487186:610098206. In both areas, the values of  $\alpha$  from our thermophysical solution are  
622 smaller than the area of unresolved materials seen in the images. Given the coarse PolyCam<sup>32</sup>  
623 resolution, it is possible that there are unmapped particles larger than  $l_s$  (but smaller than the  
624 image resolution) that our thermophysical model detects as rocks and thus do not contribute to  
625 the value of  $\alpha$ .

626

627 **Extended Data Fig. 4. The correlation between  $\Gamma_R$  and  $\alpha$  is statistically significant.** a,  
628 Spearman correlation coefficient. b, Spearman p-value; a Spearman  $p < 0.05$  indicates that the  
629 correlation between  $\Gamma_R$  and  $\alpha$  is statistically significant. The figure corresponds to the results for  
630 a value of regolith macroporosity of  $\phi = 40\%$ .

631

632 **Extended Data Fig. 5. The correlation between  $\Gamma_R$  and  $\alpha$  is robust against the choice of the**  
633 **fine-regolith macroporosity.** The results for macroporosity  $\phi = 15\%$  and  $\phi = 60\%$  have Spearman  
634 correlation coefficients  $0.56 \pm 0.06$  and  $0.58 \pm 0.06$ , probability of non-correlation  $p < 0.05$ , and are  
635 within 3 standard deviations of the best-fit values for regolith macroporosity of  $\phi = 40\%$  in 99%  
636 and 92% of the cases, respectively. The correlations are robust against removing the areas whose  
637 solutions are statistically distinct from the dataset with macroporosity  $\phi = 40\%$  (Spearman

638 correlation index:  $0.55 \pm 0.07$  and  $p < 0.05$  in 100% of 10,000 trials). The error bars correspond to  
639 1 standard deviation (Supplementary Table 1; Methods) computed on  $\sim 450$  and  $\sim 880$  samples on  
640 average. The results for a regolith macroporosity of  $\phi = 40\%$  are described in the main text  
641 (Figure 1).

642

643 **Extended Data Fig. 6. The correlation between  $\Gamma_R$  and  $\alpha$  is not an artefact of**  
644 **thermophysical modelling.** We fit model radiances emitted by a single triangular facet with  
645 zero roughness; if the thermal inertia  $\Gamma \leq \Gamma_c = 100 \text{ Jm}^{-2}\text{K}^{-1}\text{s}^{-0.5}$ , then  $\alpha = 100\%$ , and if  $\Gamma_c < \Gamma < 2,500$   
646  $\text{Jm}^{-2}\text{K}^{-1}\text{s}^{-0.5}$ , then  $\alpha = 0\%$ . We retrieve the expected step function of  $\alpha$  as a function of  $\Gamma$ ,  
647 indicating that the correlation in Figure 1 is unlikely to be an artefact of the model. The error  
648 bars correspond to 1 standard deviation computed on  $\sim 1.76 \times 10^4$  samples on average (Methods).

649

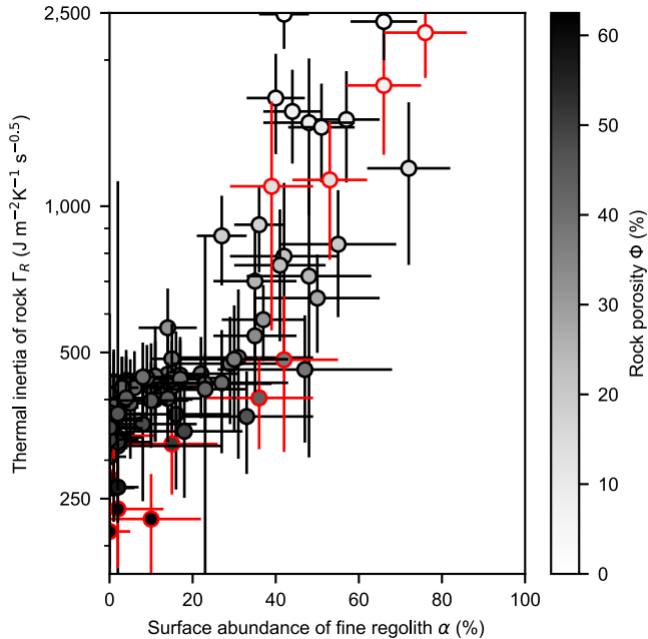
650 **Extended Data Fig. 7. The correlation between  $\Gamma_R$  and  $\alpha$  is not a geometric effect due to**  
651 **boulders' sizes.** a, PolyCam image of the surface corresponding to spots 609486110:610097198  
652 where  $\alpha$  is low probably because the spots are filled by a large, dark boulder. b, PolyCam image  
653 of the surface corresponding to spots 609495164:610106090 where  $\alpha$  does not correlate with the  
654 size of the largest boulder; this is representative of most of the surveyed areas. c, plot of  $\alpha$  as  
655 function of the percentage of the OTEs spot covered by the largest boulder on the surface. The  
656 Spearman test reveals that these two quantities have a probability of non-correlation above the  
657 critical threshold of 0.05 in 99.99% of 10,000 trials. This indicates that the  $\Gamma_R$ - $\alpha$  correlation of  
658 Figure 1 is not the result of geometric effects. The error bars in panel c correspond to 1 standard  
659 deviation (Supplementary Table 1; Methods) computed on  $\sim 670$  samples on average.

660

661 **Extended Data Fig. 8. The time required to thermally break rocks is shorter for low-**  
662 **porosity rocks than for high-porosity rocks.** We consider the asteroid to be in near-Earth space  
663 and explore a range of rotation periods corresponding to the shaded areas. The latter is to take  
664 into account changes in the current rotation periods (4.296 h and 12.1 h for Bennu and Itokawa,  
665 respectively) that these asteroids may have experienced in the past<sup>49</sup> due to the Yarkovsky–  
666 O'Keefe–Radzievskii–Paddack (YORP) effect. We estimate that in their main belt source region,  
667 at about 2.3 au from the Sun, the time to break is ~60 times longer.

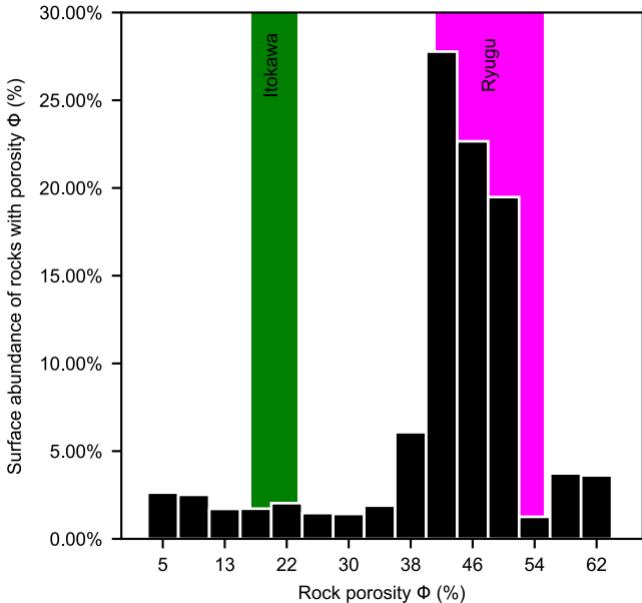
668

669 **Extended Data Fig. 9. Examples of in-situ boulder fragmentation on Bennu.** a, a 5.4 m-  
670 diameter boulder located at 22° N 157° E. b, a 5.6 m-diameter boulder located at 42° N 170° E.  
671 c, a 5.3 m-diameter boulder located at 57° N 304° E. d, a 5 m-diameter boulder located at 39° S  
672 203° E. The images are from the global mosaic<sup>32</sup> acquired by the PolyCam<sup>33</sup> imager of OCAMS.



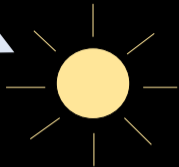


■ Benu's rocks



Diurnal illuminations cycles

drive thermal cracking



This rock is excavated and broken in situ by meteoroid impacts

This rock is compacted by meteoroid impacts

High-thermal-inertia, low-porosity rocks

Low-thermal-inertia, high-porosity rocks

Thermal cracking

Thermal cracking

